The Raman Modes of the Aurivillius Phases: Temperature and Polarization Dependence

P. R. Graves,* G. Hua,† S. Myhra,*·‡·1 and J. G. Thompson§

*AEA Industrial Technology, Harwell Laboratory, Oxfordshire OX11 ORA, United Kingdom; †Department of Physics, Monash University, Clayton, Victoria 3168, Australia; ‡Faculty of Science and Technology, Griffith University, Nathan, Queensland 4111, Australia; and §Research School of Chemistry, Australian National University, P.O. Box 4, Australian Capital Territory 2601, Australia

Aurivillius phases of order $n = 1$–4, consisting of perovskite-like $(A_{n-1}B_nO_{3n+1})^{2-}$ blocks regularly interleaved with $(Bi_2O_2)^{2+}$ sheets, have been studied by laser Raman microprobe. The trends in the Raman spectra have been correlated with the chemical and structural relationships between these phases, and have also been compared with results from other layered oxides containing perovskite-like units. Isomorphism of the $Bi_2(Mo, W)O_6$ $n = 1$ members has been confirmed. The phase and Curie transitions have been identified from the evolution of temperature-dependent spectra. Some of these transitions correlate well with previously reported results; others are reported for the first time. Single crystals of two members ($n = 1$ and 3) of the series were used to assign the Raman modes from the polarization dependence; the major features were interpreted in the context of the distortions and displacements, some of which are thought to account for the ferroelectric properties of these phases. © 1995 Academic Press, Inc.

INTRODUCTION

The Aurivillius phases were first described in 1949 (1). This large family of displacive ferroelectrics attracted considerable interest (e.g., Ref. (2)) during the 1960s and early 1970s, but interest appeared to fade after that. More recently, they have received additional attention from Withers et al. (3, 4). The latter investigation and others (5) were motivated in part by the apparent structural relationships of the Aurivillius phases with the then recently discovered Bi- and Tl-based HTSC compounds. The HTSC compounds of order $n = 1, 2, 3$ may be described as consisting of one to three slabs of perovskite-like layers, separated by a double Bi/Tl oxide layer (5). On the other hand, the Aurivillius phases of order n consist of perovskite-like blocks, $(A_{n-1}B_nO_{3n+1})^{2-}$, regularly interleaved with $(Bi_2O_2)^{2+}$ sheets (e.g., for $n = 3$ we have $Bi_4Ti_3O_{12} = [Bi_2O_2] \cdot [Bi_2Ti_3O_{10}]$). The structural refinements of an average $Fmmm$ structure can be generated by commensurate modulations; this has been described

in a series of papers (6–9). It is also convenient to think of the HTSCs as being layered, not only because of the structural relationships, but also for reasons of the highly anisotropic electronic properties. This has given additional impetus to studies of those families of oxide compounds which are both perovskite based and layered, such as the Aurivillius and the Ruddlesden–Popper phases (10, 11). The latter may be described as $n[ABO_3] \cdot [AO]$ with $n = 1, 2, 3, \ldots, \infty$, and $n = \infty$ being the perovskite end-member. Typically A is an alkaline earth species and B is a tetravalent cation. The Ruddlesden–Popper phases have received a great deal of attention in a recent series of papers (12–15). Common to all of these oxide compounds, as well as to the prototype perovskite, is the BO_6 octahedron. The principal distinctive structural features, which distinguish the different phases, are found in the layers between the perovskite slabs. Second-order variations may be due to distortions in the a–b plane, which accompany the frequently observed tetragonal-to-orthorhombic transitions (e.g., Refs. (12, 13)), as well as displacive distortions. The latter are generally features of ferroelectric crystals.

In addition to their relationship with the HTSC phases and other layered compounds, the Aurivillius phases merit investigation because of their interesting ferroelectric properties (16, 17). Current thinking suggests that the spontaneous polarization is due to a subtle interplay of several displacive mechanisms, involving rigid displacements along the "polar" axis, as well as rotations around the "polar" axis and the c-axis (17).

The present study is concerned mainly with the regularities of the Raman modes for $n = 1, 2, 3, 4$ and may be considered as a companion to similar studies of the Ruddlesden–Popper phases (12, 18) and the Bi/Tl-based HTSCs (19–21).

SYMMETRIES AND PREDICTED VIBRATIONAL MODES

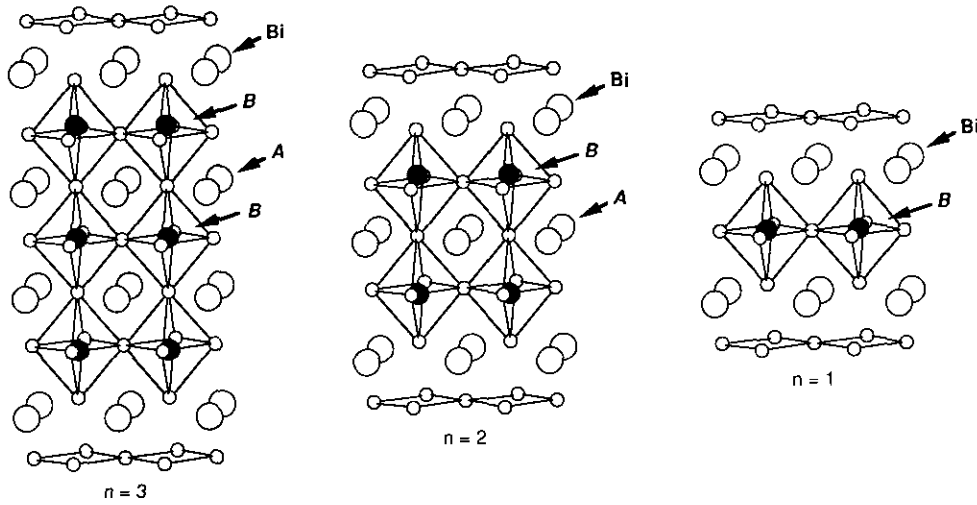It has become traditional to describe the Bravais lattices of the ferroelectric Aurivillius phases as having a

---

FIG. 1. A perspective drawing, approximately down $\langle 110 \rangle$, of the undistorted $Fmmm$ parent structures of $n = 3$ ($Bi_4Ti_3O_{12}$, A = Bi, B = Ti; $Bi_2La_2Ti_3O_{12}$, A = La, B = Ti), $n = 2$ (Bi_3TiNbO_9, A = Bi, B = Ti,Nb; $Bi_2SrTa_2O_9$, A = Sr, B = Ta), and $n = 1$ ($\gamma - Bi_2MoO_6$, B = Mo; Bi_2WO_6, B = W). Only atoms between $\frac{1}{4}c$ and $\frac{3}{4}c$ are shown.

$\sqrt{2}a_p \times \sqrt{2}a_p$ basal plane, where a_p refers to the $I4/mmm$ tetragonal prototype. Likewise, it is convenient to define $\mathbf{a} = \mathbf{a}_p + \mathbf{b}_p$ and $\mathbf{b} = -\mathbf{a}_p + \mathbf{b}_p$, and to select the space group settings (A-centered for n even, B-centered for n odd and $P2_1ab$ for $Bi_2(Mo, W)O_6$) so that the a-axis in each case coincides with the direction of the spontaneous polarization. Additional displacive modulations of the resultant $Fmmm$ "average" structure ($a \approx b \approx 3.85 \sqrt{2}$ Å, c) will then lower the symmetry to orthorhombic, or in the case of $Bi_4Ti_3O_{12}$, to monoclinic. The $n = 1, 2$, and 3 structures are shown in Fig. 1.

As a first approximation it is helpful to assign tetragonal ($I4/mmm$) symmetry to the Aurivillius phases. This corresponds to the symmetry above T_c (the ferroelectric Curie transition temperature). Likewise, the BO_6 octahedra will be assumed to be described by the O_h point group. Accordingly, one may generate the vibrational modes at $q = 0$ as shown in Tables 1, 2, and 3 for the phases of order $n = 1, 2$, and 3, respectively, where n

refers to the number of perovskite blocks. The following Raman and IR modes should be active:

$$2A_{1g}(R) + B_{1g}(R) + 3E_g(R) + 5A_{2u}(IR) + B_{2u}(IR) + 6E_u(IR), \quad \text{for } n = 1;$$

$$4A_{1g}(R) + 2B_{1g}(R) + 6E_g(R) + 7A_{2u}(IR) + B_{2u}(IR) + 8E_u(IR), \quad \text{for } n = 2;$$

$$6A_{1g}(R) + 2B_{1g}(R) + 8E_g(R) + 9A_{2u}(IR) + 2B_{2u}(IR) + 11E_u(IR), \quad \text{for } n = 3.$$

Thus there are 6, 12, and 16 Raman active modes for $n = 1, 2$, and 3, respectively. These may be visualized as shown in Fig. 2 for the A_{1g} and E_g modes. In the interest of brevity, only the A_{1g} modes are shown explicitly. As an aid to visualization of the E_g modes, these have been shown explicitly for the $n = 1$ phase in Fig. 3. The modes have been arranged in such a way as to emphasise the evolution of these from $n = 1$ to 3 with the addition of

TABLE 1
The Normal Vibrational Modes at $q = 0$ for $n = 1$ (e.g., Bi_2WO_6)

Species	W	O_{11}, O_{12}	O_{31}, O_{32}	Bi_1, Bi_2	O_{21}, O_{22}	Raman
A_{1g}			$z_1 - z_2$	$z_1 - z_2$		$x^2 + y^2, z^2$
B_{1g}					$z_1 - z_2$	$x^2 - y^2$
E_g			$x_1 - x_2$	$x_1 - x_2$	$x_1 - x_2$	(xz, yz)
			$y_1 - y_2$	$y_1 - y_2$	$y_1 - y_2$	
A_{2u}	z	$z_1 + z_2$	$z_1 + z_2$	$z + z_2$	$z_1 + z_2$	
B_{2u}		$z_1 - z_2$				
E_u	x	x_1, x_2	$x_1 + x_2$	$x_1 + x_2$	$x_1 + x_2$	
	y	y_1, y_2	$y_1 + y_2$	$y_1 + y_2$	$y_1 + y_2$	

TABLE 2
The Normal Vibrational Modes at $q = 0$ for $n = 2$ (e.g., Bi_3TiNbO_9)

Species	Ti_1, Ti_2	O	O_{21}, O_{22}	O_{41}, O_{42}, O_{43}, O_{44}	Bi_{21}, Bi_{22}	O_{31}, O_{32}	Bi	Raman
A_{1g}	$z_1 - z_2$		$z_1 - z_2$	$z_1 + z_2 - z_3 - z_4$	$z_1 - z_2$			$x^2 + y^2$, z^2
B_{1g}				$z_1 - z_2 - z_3 + z_4$		$z_1 - z_2$		$x^2 - y^2$
E_g	$x_1 - x_2$		$x_1 - x_2$	$x_1 - x_3$, $x_2 - x_4$	$x_1 - x_2$	$x_1 - x_2$		(xz, yz)
	$y_1 - y_2$		$y_1 - y_2$	$y_1 - y_3$, $y_2 - y_4$	$y_1 - y_2$	$y_1 - y_2$		
A_{2u}	$z_1 + z_2$	z	$z_1 + z_2$	$z_1 + z_2 + z_3 + z_4$	$z_1 + z_2$	$z_1 + z_2$	z	
B_{2u}				$z_1 - z_2 + z_3 - z_4$				
E_u	$x_1 + x_2$	x	$x_1 + x_2$	$x_1 + x_3$, $x_2 + x_4$	$x_1 + x_2$	$x_1 + x_2$	x	
	$y_1 + y_2$	y	$y_1 + y_2$	$y_1 + y_3$, $y_2 + y_4$	$y_1 + y_2$	$y_1 + y_2$	y	

TABLE 3
The Normal Vibrational Modes at $q = 0$ for $n = 3$ (e.g., $Bi_4Ti_3O_{12}$)

Species	Bi_{11}, Bi_{12}	Bi_{21}, Bi_{22}	Ti_1	Ti_{21}, Ti_{22}	O_{11}, O_{12}	O_{21}, O_{22}	O_{31}, O_{32}	O_{41}, O_{42}	O_{51}, O_{52}, O_{53}, O_{54}	Raman
A_{1g}	$z_1 - z_2$	$z_1 - x_2$		$z_1 - z_2$			$z_1 - z_2$	$z_1 - z_2$	$z_1 + z_2 - z_3 - z_4$	$x^2 + y^2$, z^2
B_{1g}						$z_1 - z_2$			$z_1 - z_2 - z_3 + z_4$	$x^2 - y^2$
E_g	$x_1 - x_2$	$x_1 - x_2$		$x_1 - x_2$		$x_1 - x_2$	$x_1 - x_2$	$x_1 - x_2$	$x_1 - x_3$, $x_2 - x_4$	(xz, yz)
	$y_1 - y_2$	$y_1 - y_2$		$y_1 - y_2$		$y_1 - y_2$	$y_1 - y_2$	$y_1 - y_2$	$y_1 - y_3$, $y_2 - y_4$	
A_{2u}	$z_1 + z_2$	$z_1 + z_2$	z	$z_1 + z_2$	$z_1 + z_2$	$z_1 + z_2$	$z_1 + z_2$	$z_1 + z_2$	$z_1 + z_2 + z_3 + z_4$	
B_{2u}					$z_1 - z_2$				$z_1 - z_2 + z_3 - z_4$	
E_u	$x_1 + x_2$	$x_1 + x_2$	x	$x_1 + x_2$	x_1, x_2	$x_1 + x_2$	$x_1 + x_2$	$x_1 + x_2$	$x_1 + x_3$, $x_2 + x_4$	
	$y_1 + y_2$	$y_1 + y_2$	y	$y_1 + y_2$	y_1, y_2	$y_1 + y_2$	$y_1 + y_2$	$y_1 + y_2$	$y_1 + y_3$, $y_2 + y_4$	

A_{1g}
(E_g) (top)

Labels (top): Bi2; O21,O22; Bi1; O31; •W O11,O12; O32; Bi2; Bi1

A_{1g}
(E_g) (middle)

Labels (middle): Bi22; O31,O32; Bi21; O21; •Ti1 O41,O42; O,Bi; •Ti2 O43,O44; O22; Bi22; O31,O32; Bi21

A_{1g}
(E_g) (lower)

Labels (lower): Bi22; O21,O22; Bi21; O41; •Ti21 O51,O52; O31,Bi11; •Ti1 O11,O12; O32,Bi12; •Ti22 O53,O54; O42; Bi22; O21,O22; Bi21
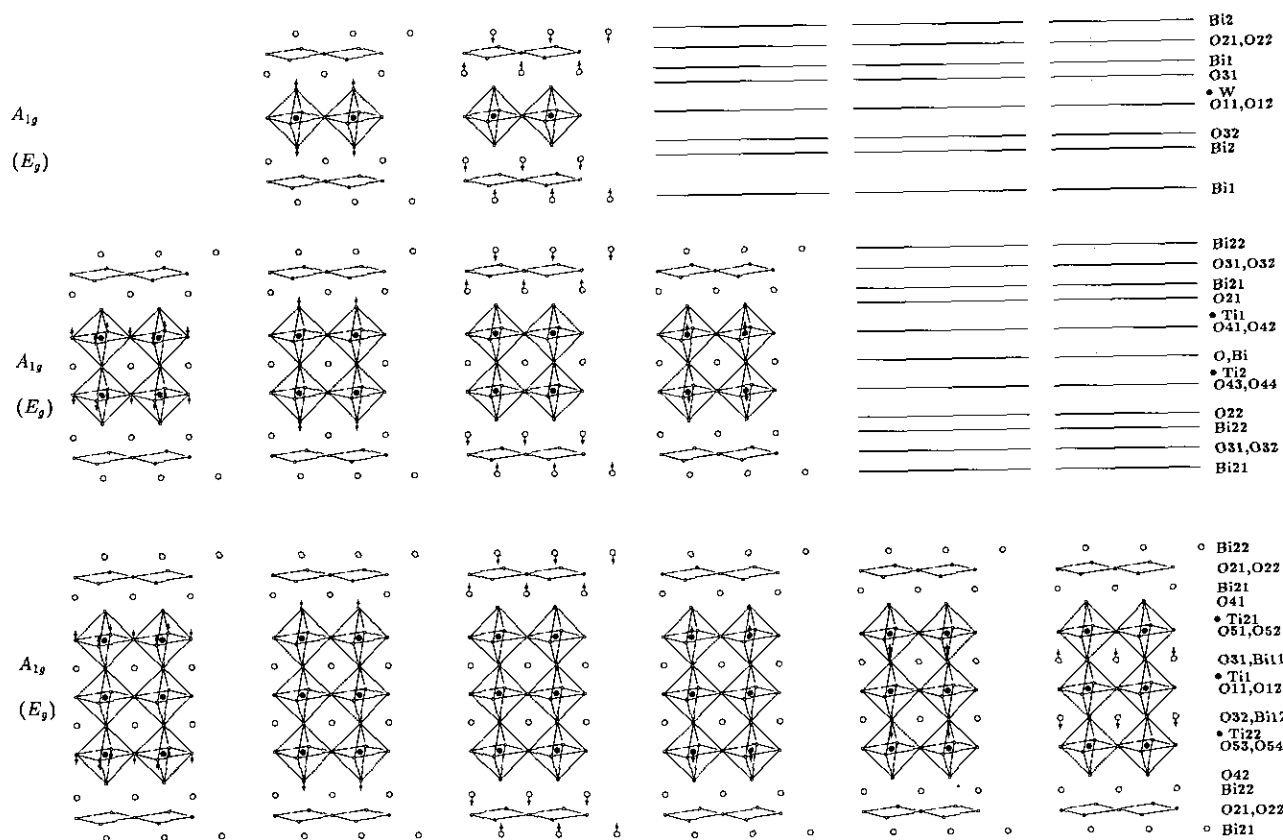
FIG. 2. A montage of pictorial representations of the predicted A_{1g} and E_g Raman modes for $n = 1$ (top), 2 (middle), and 3 (lower) Aurivillius phases. The cation and anion labeling is indicated along the vertical scale.
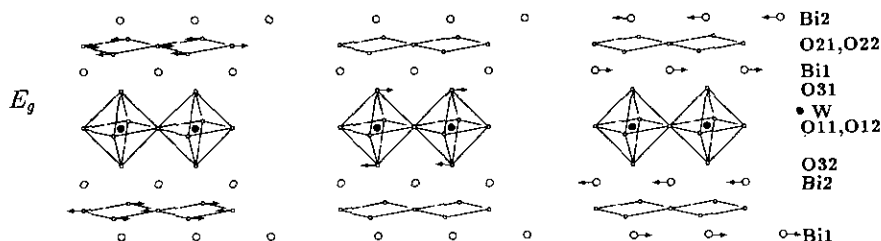
FIG. 3. The expected E_g modes for the $n = 1$ phase.

BO_6 octahedral layers. Figure 4 shows the B_{1g} and corresponding E_g modes. The *ungerade* modes are of peripheral interest in this study and are not shown.

EXPERIMENTAL DETAILS

(a) Specimen Synthesis and Characterization

The materials studied by Raman spectroscopy in the present investigation were investigated previously by single-crystal and/or powder X-ray diffraction, transmission electron microscopy, and X-ray photoelectron spectroscopy. With the exception of γ-Bi_2MoO_6, which was prepared by a coprecipitation method (22), the specimens were all prepared by solid-state reaction of the component oxides, and their synthesis and characterization are described elsewhere: Bi_2WO_6 (8), $Bi_2SrTa_2O_9$ (9), Bi_3TiNbO_9 (7), $Bi_4Ti_3O_{12}$ (6), and $Bi_4BaTi_4O_{15}$ (5). The $Bi_2La_2Ti_3O_{12}$ phase, which is isostructural with the paraelectric form of $Bi_4Ti_3O_{12}$, was prepared by reaction of Bi_2O_3, La_2O_3, and TiO_2, all 99.9% purity, in an open platinum crucible with a final annealing temperature of 1100°C. All specimens were determined to be single phase by X-ray powder diffraction.

(b) Raman Procedures

The analyses were carried out with a laser Raman microprobe (LRM) with true backscatter configuration. The general features of the instrument have been described elsewhere (23) and the general procedures were in accord with established practice (e.g., Refs. (12, 19)). Parallel detection was effected with a two-dimensional liquid-nitrogen-cooled charge-coupled array, 420 × 600 pixels (ATI CCD Imaging System, Wright Instruments, Ltd), with an overall quantum efficiency of 70%. Data acquisition was under computer control. The exciting source was the 514.5-nm line from an argon ion laser which was filtered by a premonochromator in order to remove unwanted plasma lines. The incident power was focussed into a 2-μm spot by an X40 objective lens, and the backscatter collection efficiency was determined by its numerical aperture of 0.65. The incident power was limited

to less than 1 mW (equivalent to a power density of approximately 10^8 W/m²).

The directions of the E-vector for incident and scattered light were defined by a half-wave plate and a po-
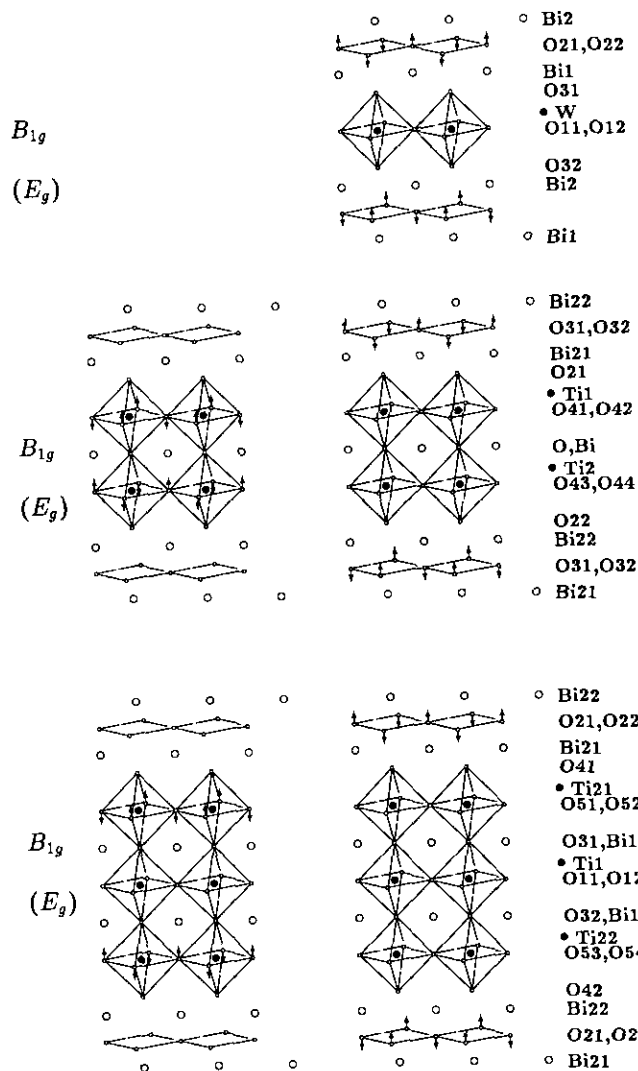

FIG. 4. A montage of the predicted B_{1g} and E_g Raman modes for $n = 1$ (top), 2 (middle), and 3 (lower) Aurivillius phases.

lariser, respectively. The orientations were calibrated with the use of a liquid carbon tetrachloride specimen. The geometry of the LRM constrained the polarisation dependences to $i(jk)i$. (We use the Porto notation where i and i indicate the propagation directions for incident and scattered light, and j and k are the directions of the E-vector for incident and scattered light). The coodinate system was fixed in the specimen with z parallel to the c-axis, and with x and y in the $a-b$ plane. As a result of the backscatter configuration for the LRM it was impossible to carry out measurements, for $j = k$, much below 150 cm^{-1}, due to the high intensity of elastically scattered radiation.

Temperature dependent measurements were carried out using a hot/cold stage (Stanton Redcroft HSM-5) with a U.T.P. controller, resulting in set-point stability of better than 1°C. The appearance of the high-temperature spectra (above 300°C) suggests that blackbody radiation from the cavity of the hot stage became an increasingly important contribution to the background intensity.

RESULTS

(a) General Trends

A series of spectra obtained for powder specimens is shown in Fig. 5. These results illustrate the trends for n = 1, 2, 3, and 4, as well as the effects of cation substitution within the BO$_6$ octahedra (for Bi$_2$WO$_6$ versus Bi$_2$MoO$_6$, and for Bi$_2$SrTa$_2$O$_9$ versus Bi$_3$TiNbO$_9$). Similarly, the effects of cation substitution in the interstices of the BO$_6$ blocks are exemplified by the results for the n = 2 and 3 members. The results in Fig. 5 are representative of the typical outcomes of Raman interactions for random angles of propagation and polarisation vis à vis lattice axes (i.e., several randomly oriented grains were within the interaction volume).

(b) Temperature Dependence

The evolution of the Raman spectra with temperature for the two n = 1 specimens is illustrated in Figs. 6 and 7. Likewise, representative results for the n = 2, 3 phases are shown in Fig. 8. The temperature set-points were established in random order. The integrity of the specimens against heating to elevated temperatures in air was checked by acquiring room-temperature spectra before and after heat treatment. The specimens were synthesized at temperatures in excess of 1000°C. All analyses were carried out in air (i.e., under oxydising conditions). Accordingly, one would expect the phases to remain stable toward oxygen loss.

(c) Single Crystals

Analyses of single-crystal specimens of n = 1 (Bi$_2$WO$_6$) and n = 3 (Bi$_4$Ti$_3$O$_{12}$) phases were carried out with polar-
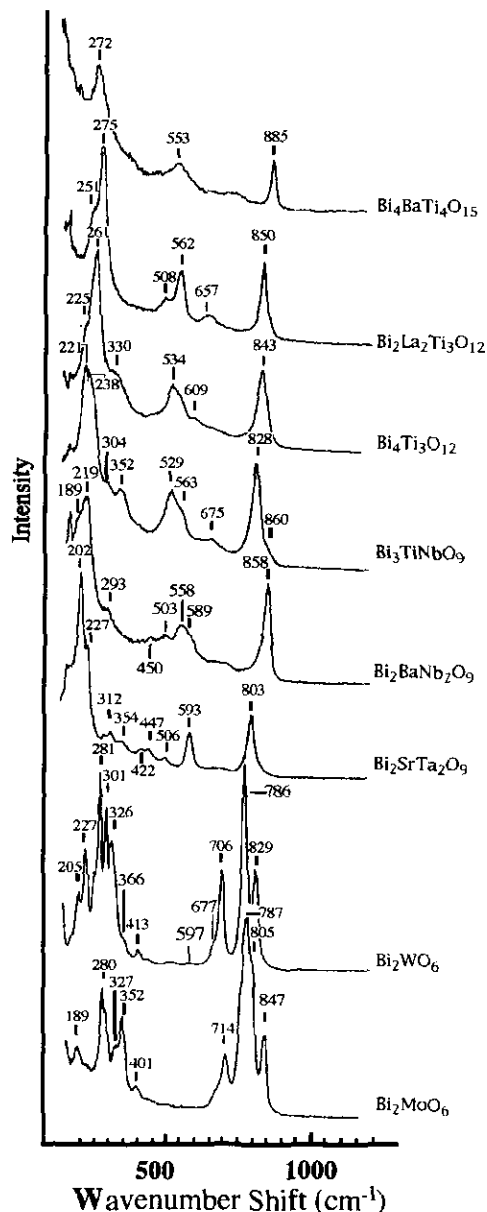

FIG. 5. Raman spectra for n = 1, 2, 3, and 4 Aurivillius phases. These results were obtained for powder specimens at ambient temperature.

ization-dependent measurements in an attempt to assign spectral features to particular modes.

The Bi$_4$Ti$_3$O$_{12}$ were large platey crystals having (001) orientation, with visible twin boundary planes [110] aligned with the c-axis. Figure 9 shows the spectra for typical polarization-dependent results for propagation along the c-axis (incident on a large flat face) and perpendicular to the c-axis (incident on a fracture face). The orientation of the twin boundaries and their proximity to the point of analysis did not appear to affect the results.

The Bi$_2$WO$_6$ crystals were separated out from intergrown agglomerates. The most common crystals were
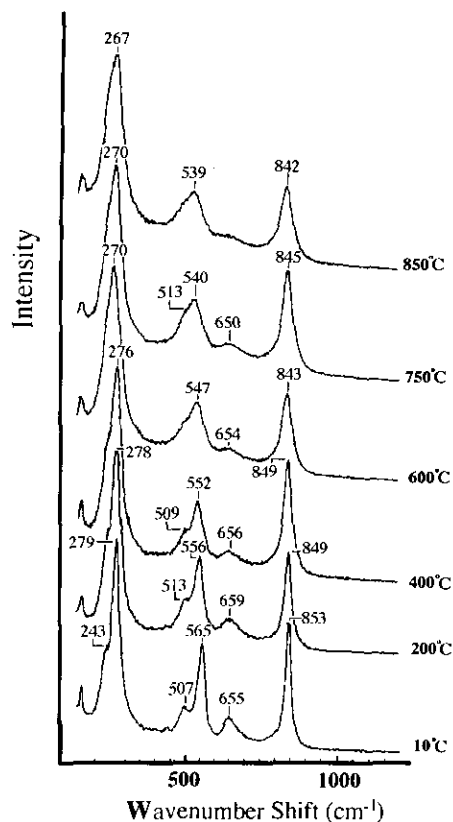
FIG. 6. Temperature dependence of the Raman spectra for a powder specimen of the Bi_2WO_6 phase.

Similarly, for orthorhombic symmetry (D_{2h}) the following criteria can be generated:

$$z(xx)\underline{z}, \ y(xx)\underline{y} \ \leftrightarrow A_{1g'}$$

$$z(yy)\underline{z}, \ x(yy)\underline{x} \ \leftrightarrow A_{1g''}$$

$$x(zz)\underline{x}, \ y(zz)\underline{y} \ \leftrightarrow A_{1g'''}$$

$$z(xy)\underline{z}, \ z(yx)\underline{z} \ \leftrightarrow B_{1g}$$

$$y(xz)\underline{y}, \ y(zx)\underline{y} \ \leftrightarrow B_{2g}$$

$$x(yz)\underline{x}, \ x(zy)\underline{x} \ \leftrightarrow B_{3g}.$$

The modes being generated by the heavier cations tend to exhibit small wavenumber shifts, while the lighter anions generate modes with larger shifts. The backscatter configuration of the LRM imposes a high background below 150 cm^{-1} from the elastically scattered photons; the modes in the spectra in the current experiments therefore are likely to be stimulated by the oxygen sublattice.

Previous work on the Ruddlesden–Popper phases (12) and on the $CaTiO_3$ perovskite endmember (25) have tentatively identified several of the major TiO_6 modes. These

blocks with one large face. Figure 10 shows the spectra for various directions of the propagation and polarization vectors. The assignments of orientations vis à vis unit cell directions were inferred by identifying major A_{1g} and E_g modes in the temperature-dependent spectra in Fig. 6, and by identifying configurations which resulted in invariant spectra under interchange of directions for the incident and scattered polarization vectors.

DISCUSSION

The Raman-active vibrational modes and the polarization tensors for the 32 crystal classes can be found in the literature (e.g., Ref. (24)). In the present case for tetragonal symmetry (D_{4h}) it is straightforward to show that (assuming that the x, y, z axes are aligned with the **a, b, c** crystal axes):

$$z(xx)\underline{z}, \ z(yy)\underline{z}, \ x(yy)\underline{x}, \ y(xx)\underline{y} \ \leftrightarrow A_{1g'} + B_{1g}$$

$$x(zz)\underline{x}, \ y(zz)\underline{y} \qquad\qquad \leftrightarrow A_{1g''}$$

$$x(zy)\underline{x}, \ x(yz)\underline{x}, \ y(zx)\underline{y}, \ y(xz)\underline{y} \ \leftrightarrow E_g$$

$$z(yx)\underline{z}, \ z(xy)\underline{z} \qquad\qquad \leftrightarrow B_{2g}.$$

FIG. 7. Temperature dependence of the Raman spectra for a powder specimen of the Bi_2MoO_6 phase.

FIG. 8. Temperature dependence of the Raman spectra for a powder specimen of the $Bi_2La_2Ti_3O_{12}$ phase.

FIG. 9. Raman spectra of a single-crystal $Bi_4Ti_3O_{12}$ specimen for specific directions of propagation and polarization vetors, and at ambient temperature.

include several E_g modes (which split into B_{2g} and B_{3g} modes at the tetragonal-to-orthorhombic transition) in the range 200–400 cm^{-1} which have been ascribed to O–Ti–O bending. A major mode at 470–490 cm^{-1} has been assigned E_g character (this also splits into B_{2g} and B_{3g} modes) and described as a Ti–O torsional mode. A prominent feature at 650 cm^{-1} exhibits A_{1g} character and has been associated with the Ti–O symmetric stretch.

It is plausible to assign the symmetric stretching of the BO_6 octahedra to the prominent feature at 780–850 cm^{-1} for $Bi_2(Mo, W)O_6$; these modes are seen to shift gradually to higher wave numbers for $n = 2, 3$, and 4 (Fig. 5). The three $n = 2$ compounds have the B-sites occupied by Ta cations and by the lighter Ti and Nb species, respectively. In the latter case, the stretching mode is shifted upward by 55 cm^{-1}, in accordance with the lower reduced mass of the octahedra. The corresponding situation for the two $n = 3$ phase shows nearly identical shifts (843 vis à vis 850 cm^{-1}), as expected, since the B-site species are identical.

The corresponding E_g modes involving opposing excursions of the external apical oxygen atoms of the octahedra are twofold degenerate for a tetragonal cell (along
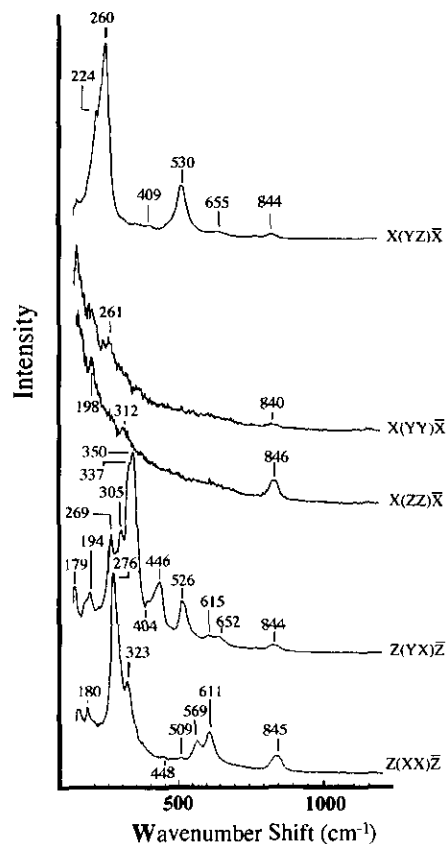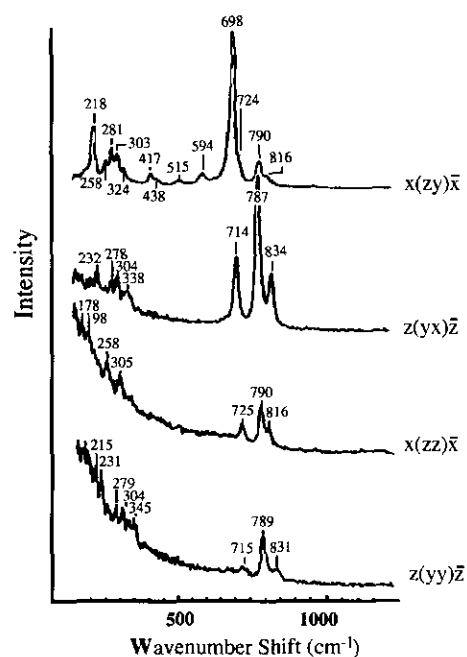

FIG. 10. Raman spectra of a single-crystal Bi_2WO_6 specimen for specific directions of propagation and polarization vectors, and at ambient temperature.

x- and y-axes). The shifts of these modes are likely to be much lower than for the corresponding A_{1g} modes (cf. 663 and 508 cm^{-1} for the PbTiO$_3$ perovskite (26), and 630 and 490 cm^{-1} for the tetragonal Ruddlesden–Popper phases $(Ca_xSr_{1-x})_4Ti_3O_{10}$ (12). Accordingly, the relatively strong features at 593, 558/589, and 529/563 cm^{-1} ($n = 2$ phases), at 534/559 and 508/562 cm^{-1} ($n = 3$ phases), and at 517/592 cm^{-1} (for the $n = 4$ phase) can be assigned to these modes. The splitting into two components is consistent with orthorhombic distortion, generating $E_g \rightarrow B_{2g} + B_{3g}$ splitting, for most of these phases. It must be emphasised that the spectra in Fig. 5 were obtained at room temperature; the significance of this point will become apparent in the discussion below.

The vibrational spectra of $A_2(Mo, W)O_6$ compounds have been investigated in a previous study (27); the results for the $Bi_2(Mo, W)O_6$ phases are particularly relevant to the present study. The agreement is excellent in the case of the Bi_2WO_6 member. Conversely, while close correspondence is found between the spectra for the Mo and W members in the present study, Fig. 5, the previous work (27) suggested major differences; these were interpreted in the context of the coordination of the B-site. The good correspondence is in accord with expectations since structure determinations by XRD and TEM indicate isomorphism between the two members. The effects of Mo for W substitution on the Raman spectra should be relatively minor since the B-site location is a center of symmetry in the undistorted average structure, and since the size of the BO_6 octahedron is relatively insensitive toward the substitution. However, the plethora of modes, even above 150 cm^{-1}, suggests that as a minimal requirement there is a need to invoke orthorhombic distortion.

The assumption of isomorphism for the two $n = 1$ members is reenforced by the temperature-dependent results in Figs. 6 and 7, although the temperature scaling in the evolution of the spectra is different. The high-temperature spectra may be interpreted in the context of tetragonal symmetry. Accordingly, the features at 796 and 781 cm^{-1} for $B = W$ and Mo, respectively, are presumably A_{1g} modes, and represent the symmetric stretch of the BO_6 octahedron. The modes between 270 and 360 cm^{-1} for both members will then have E_g character (plausibly due to the rocking mode of the octahedron). Likewise, the features at 205/227 cm^{-1} for $B = W$ have E_g character, as may have the equivalent structure at 183 cm^{-1} for the $B = Mo$ member (possibly the transverse motion of the cations in the Bi-layer). The remaining features, at 706 cm^{-1} ($B = W$, Mo) must also have A_{1g} character and be due to orthorhombic distortion of the octahedron; a similar assignment may be made for the 829 and 843 cm^{-1} modes.

The Bi_2MoO_6 member exhibits two structural transi-

tions. The first of these takes place between 300 and 350°C; the major E_g mode at ≈ 300 cm^{-1} splits into two components separated by 50 cm^{-1}. Below 150°C these two components both split yet again with separations of 15–20 cm^{-1}. Above 350°C the A_{1g} modes coalesce into a single strong mode at 876 cm^{-1}, albeit with a shoulder at 768 cm^{-1}, suggesting cubic symmetry for the BO_6 octahedron. The other $n = 1$ member (Bi_2WO_6) appears to follow a similar scheme with the analogous E_g modes first splitting into two components at around 600°C; these components then split yet again at the second transition at 300–400°C.

The evolution of the complex structures between 650 and 900 cm^{-1} suggests that as well as a tetragonal-to-orthorhombic transition there must be additional lowering of symmetry, as implied by the observed room-temperature space group $P2_1ab$. This interpretation has the additional merit of accounting for the two times sequential doubling of the original E_g modes.

The interpretation of the temperature dependence of the $n = 2, 3,$ and 4 spectra, an example of which is shown in Fig. 8 for the $Bi_2La_2Ti_3O_{12}$ phase, is somewhat more straightforward. For instance, the sharp modes in the range 800–900 cm^{-1} remain intact over the whole temperature range, and therefore have unequivocal A_{1g} character, due to the stretching of the BO_6 octahedra. The major modes in the range 450–600 cm^{-1} have E_g character at high temperatures, and are found to split at lower temperatures. Other major features between 200 and 300 cm^{-1} also show E_g character at high temperatures and exhibit splitting nearer to room temperature. There are additional modes with E_g character for Bi_3TiNbO_9 and $Bi_2Sr Ta_2O_9$, exhibiting similar splitting at 300–400 cm^{-1}. A mode with A_{1g} character can be found at 160 cm^{-1} for the $Bi_2SrTa_2O_9$ member, and at a similar shift for the $Bi_2 La_2Ti_3O_{12}$ member.

The montage in Fig. 9 shows the dependence at room temperature of the Raman excitations in $Bi_4Ti_3O_{12}$ on directions of the E-vector for incident and scattered light. Assuming tetragonal symmetry as a first approximation, the character of the modes are predicted above. Also, the interpretations based on the results in Fig. 9 ought to be consistent with the conclusions drawn from the temperature-dependent data. Accordingly it can be seen that the modes at 569, 611, and 845 cm^{-1} clearly have A_{1g} character. The modes at 224, 260, and 530 cm^{-1} have $B_{2g} + B_{3g}$ character, while the features at 337, 446, and 652 cm^{-1} have B_{1g} character. Another major structure at 220–270 cm^{-1} (for $x(yz)\underline{x}$ polarization) is likely to be of $B_{2g} + B_{3g}$ origin due to the lifting of E_g degeneracies, arising from orthorhombic distortion. These conclusions are in general accordance with the temperature-dependent results. The interpretations, based on results from temperature and polarization dependence, for Bi_2WO_6 and $Bi_4Ti_3O_{12}$

TABLE 4
Mode Assignments

Bi$_2$WO$_6$		Bi$_4$Ti$_3$O$_{12}$	
Feature	Character	Feature	Character
		845	A_{1g}
831	A_{1g}		
816	A_{1g}		
789	A_{1g}		
724	A_{1g}		
714	B_{1g}		
698	B_{2g}/B_{3g}		
		652	B_{1g}
		611	A_{1g}
594	B_{2g}/B_{3g}		
		569	A_{1g}
		530	B_{2g}/B_{3g}
515	B_{2g}/B_{3g}		
		446	B_{1g}
438	$B_{2g} + B_{3g}$		
417	$B_{2g} + B_{3g}$		
		350	B_{1g}
		337	B_{1g}
324	$B_{2g} + B_{3g}$	323	A_{1g}
303	$B_{2g} + B_{3g}$	305	
281	$B_{2g} + B_{3g}$		
		276	A_{1g}
		269	
258	$B_{2g} + B_{3g}$	260	$B_{2g} + B_{3g}$
227	$B_{2g} + B_{3g}$	224	$B_{2g} + B_{3g}$
218	$B_{2g} + B_{3g}$		
205	$B_{2g} + B_{3g}$		
		194	
		180	

are summarized in Table 4; some of the assignments are tentative, however.

Three major types of displacive distortions have been identified by Withers et al. (18). These include:

• An F2mm type which can be generated by a rigid shift along the a direction of the B_nO_{3n+1} subunits (i), a motion back in the opposite direction of the B cations vis à vis the oxygen octahedral cage (ii), and finally a rigid shift along a of the oxygen sublattice within the Bi$_2$O$_2$ layer (iii). It is atomic displacements with F2mm symmetry which give rise to the observed spontaneous polarization (P_S) along a in all the Aurivillius phases. The magnitude of P_S depends on the relative magnitude of (i)–(iii).

• A type (Bmab for n odd, or Amam for n even) consisting of alternating rotations of the octahedra about axes parallel to a. The angles of rotation are in the range 8.6–10.3°.

• A type (resulting in symmetries of the kinds Bbab and Bbam for n = 3, Abam for n = 2, and Abam and Bbam for n = 1) consisting of rotations of the octahedra

about axes parallel to c. The angles of rotation are in the range 6.5°–9.1°. In Bi$_4$Ti$_3$O$_{12}$, however, displacive distortions of Bbab and Bbam symmetry have opposite signs on one octahedron, so that the net angle of rotation is only 1.7°.

The evolution with temperature of the Raman spectra ought to reflect successive transformations whereby the symmetries are raised from those described above to the undistorted, average structure with I4/mmm. symmetry. The quenching of the F2mm distortions, in particular, should be correlated with the ferroelectric-to-paraelectric transition, in the context of the current picture. Information available from the literature on the phase transitions, whether structural and/or ferroelectric, is limited to a small number of the Aurivillius phases: Bi$_2$WO$_6$ (288?, 935, and 1235 K), Bi$_2$SrTa$_2$O$_9$ (583 and 843 K), Bi$_3$TiNbO$_9$ (1023 and 1223 K), and Bi$_4$Ti$_3$O$_{12}$ (775 and 948 K). The question mark attached to the 288 K transition refers to an ambiguous assignment in the literature (see (30)). These results have been collated in Table 5. Likewise, the estimated temperatures at which Raman-active phase transitions take place have been included. There is good agreement, within the large experimental uncertainties of the Raman measurements, between the present results and those in the literature. It should be noted that tem-

TABLE 5
Transition Temperatures

Phase	Transitions[a]				
Bi$_2$WO$_6$	T$_P$(?)		T$_R$	T$_R$ T$_P$	T$_P$
Bi$_2$MoO$_6$	T$_R$	T$_R$ T$_R$			
Bi$_2$SrTa$_2$O$_9$		T$_R$ T$_P$	T$_P$		
Bi$_2$BaNb$_2$O$_9$		No Data			
Bi$_3$TiNbO$_9$		T$_R$		T$_R$ T$_P$	T$_c$
Bi$_4$Ti$_3$O$_{12}$			T$_P$ T$_R$	T$_c$ T$_R$	
Bi$_2$La$_2$Ti$_3$O$_{12}$			T$_R$		
Bi$_4$BaTi$_4$O$_{15}$		No Data			

	300	500	700	900	1100

Temperature (K)

[a] The transition temperatures refer to results from the present experiments (boldface type and R subscripts) and from the literature (normal type. P = Phase and C = Curie).

peratures in excess of 1100 K were not accessable with the available hot cell, and would be subject to masking by blackbody radiation, in any case. In the case of $Bi_4Ti_3O_{12}$, we find Raman transitions which correspond well to the reported T_c at 948 K (28) and a known phase transition at 775 K (29). However, we do not find any convincing evidence for a reported transition at approximately 290 K for Bi_2WO_6 (30). There is inconclusive evidence, however, for this being an electronic transition since the intensities of E_g-derived modes are suppressed relative to those of the A_g modes below room temperature.

The known T_c transition at 948 K for $Bi_4Ti_3O_{12}$ is correlated with a Raman-active transition at a similar temperature. The main attribute of this transition is the quenching-out of the structure in the range 500–650 cm^{-1} over the temperature range 930–970 K. A similar phenomenon can be identified for Bi_3TiNbO_9 at 870–970 K (450–600 cm^{-1}), which also correlates with a known structural transition.

The sequence of spectra in Fig. 10 shows the dependence of the Raman excitations in Bi_2WO_6 on directions of the E-vector for incident and scattered light. The conclusions based on the results in Fig. 6 were used to identify tentatively the c-axis orientation, and to justify the initial assumption of approximate tetragonal symmetry. Accordingly, we have assigned A_{1g} character to the major modes at 725, 790, 816, and 831 cm^{-1} for the $z(yy)\underline{z}$ and $x(zz)\underline{x}$ configurations; these features are relatively less prominent due to the high elastic background. A B_{1g} mode can be found at 714 cm^{-1} for $z(yx)\underline{z}$. The origin of the two relatively strong features at 787 and 834 cm^{-1} for $z(yx)\underline{z}$ is uncertain. Possibly these are due to leakage of A_{1g} modes (cf. 790 and 831 cm^{-1} for $z(yy)\underline{z}$). The relative prominence may be due, in part, to the much lower background of elastically scattered intensity for configurations with perpendicular polarization vectors, with additional effects due to the relative magnitudes of the terms in the polarization tensor. As well, the Aurivillius phases are highly directional; one would expect the anisotropic electronic structure to affect scattering intensities; the latter has the effect of changing the depth of the interaction volume as a function of the direction of incident propagation vector. An alternative explanation may be that these are simply additional B_{1g} modes with shifts nearly degenerate with those of the relevant A_{1g} features. The $x(zy)\underline{x}$ configuration reveals E_g modes, or more likely $B_{2g} + B_{3g}$ structures which result from orthorhombic distortion. The plethora of modes and the appearance of a B_{1g} feature are inconsistent with tetragonal symmetry, and even with orthorhombicity as inferred above. At a very minimum additional lowering of symmetry is required—possibly arising from asymmetric rotations of

the BO_6 octahedra in successive blocks along the c-axis, and around axes perpendicular to the c-axis. This would permit a B_{1g} mode as well as additional A_{1g} vibrations. A similar mechanism has been identified in the case of the (Ca, Sr)TiO$_3$ perovskite and the related Ruddlesden–Popper phases (14, 15). It must be emphasised that these assignments and inferences are tentative and require confirmation from detailed structural analyses. Similar features have been observed for very small and poorly formed crystallites of the isomorphous Bi_2MoO_6 phase.

REFERENCES

1. B. Aurivillius, *Ark. Kemi* **1**, 463 (1949).
2. E. C. Subbarao, *Ferroelectrics* **5**, 267 (1973).
3. R. L. Withers, J. G. Thompson, L. R. Wallenberg, J. D. Fitz Gerald, J. S. Anderson, and B. G. Hyde, *J. Phys. C.* **21**, 6067 (1988).
4. R. L. Withers, J. S. Anderson, B. G. Hyde, J. G. Thompson, L. R. Wallenberg, J. D. Fitz Gerald, and A. M. Stewart, *J. Phys. C.* **21**, L417 (1988).
5. A. E. Bocquet, J. F. Dobson, P. C. Healy, S. Myhra, and J. G. Thompson, *Int. J. Mod. Phys. B* **3**, 455 (1989).
6. A. D. Rae, J. G. Thompson, R. L. Withers, and A. C. Willis, *Acta Crystallogr. Sect. B* **46**, 474 (1990).
7. J. G. Thompson, A. D. Rae, R. L. Withers, and D. C. Craig, *Acta Crystallogr. Sect. B* **47**, 174 (1991).
8. A. D. Rae, J. G. Thompson, and R. L. Withers, *Acta Crystallogr. Sect. B* **47**, 870 (1991).
9. A. D. Rae, J. G. Thompson, and R. L. Withers, *Acta Crystallogr. Sect. B* **48**, 418 (1992).
10. S. N. Ruddlesden and P. Popper, *Acta Crystallogr.* **10**, 538 (1957).
11. S. N. Ruddlesden and P. Popper, *Acta Crystallogr.* **11**, 54 (1958).
12. P. R. Graves, S. Myhra, K. Hawkins, and T. J. White, *Physica C* **181**, 265 (1991).
13. S. Myhra, K. Hawkins, T. J. White, and J. C. Riviere, *J. Mater. Res.* **7**, 482 (1992).
14. K. Hawkins and T. J. White, *Philos. Trans. R. Soc. London* **336**, 541 (1991).
15. M. M. Elcombe, E. H. Kisi, K. D. Hawkins, T. J. White, and P. Goodman, *Acta Crystallogr. Sect. B* **47**, 305 (1991).
16. R. E. Newnham, R. W. Wolfe, and J. P. Dorrian, *Mater. Res. Bull.* **6**, 1029 (1971).
17. R. L. Withers, J. G. Thompson, and A. D. Rae, *J. Solid State Chem.* **94**, 404 (1991).
18. G. Burns, F. H. Dacol, G. Kliche, W. Konig, and M. W. Shafer, *Phys. Rev. B* **37**, 3381 (1988).
19. P. R. Graves and S. Myhra, submitted for publication.
20. D. M. Krol, M. Stavola, L. F. Schneemeyer, J. V. Waszczak, and S. A. Sunshine, *J. Opt. Soc. Am. B* **6**, 448 (1989).
21. J. R. Ferraro and V. A. Maroni, *Appl. Spectrosc.* **44**, 351 (1990).
22. J. G. Thompson, S. Schmid, R. L. Withers, A. D. Rae, and J. D. Fitz Gerald, *J. Solid State Chem.* **101**, 309 (1992).

23. D. J. Gardiner, M. Bowden, and P. R. Graves, *Philos. Trans. R. Soc. London Ser. A* **320**, 295 (1986).

24. G. Turrell, "Infrared and Raman Spectra of Crystals," Appendix G. Academic Press, London, 1972.

25. U. Balachandran and N. G. Eror, *Solid State Commun.* **44**, 815 (1982).

26. R. E. Cohen, *Nature* **358**, 136 (1992).

27. J. H. G. Bode, H. R. Kuut, M. A. J. Th. Lahey, and G. Blasse, *J. Solid State Chem.* **8**, 114 (1973).

28. J. F. Dorrian, R. E. Newnham, D. K. Smith, and M. I. Kay, *Ferroelectrics* **3**, 17 (1971).

29. S. E. Cummins and L. E. Cross, *J. Appl. Phys.* **39**, 2268 (1968).

30. S. Ehara, T. Hattori, J. Tanaka, M. Tsukioka, K. Muramatsu, and M. Shimazu, *Jpn. J. Appl. Phys.* **25**, 1749 (1986).